Journal of
Micro/Nanolithography,
MEMS, and MOEMS

Nanolithography.SPIEDigitalLibrary.org

Free energy of defects in chemoepitaxial block copolymer directed self-assembly: effect of pattern density and defect position

Benjamin D. Nation
Caleb L. Breaux
Peter J. Ludovice
Clifford L. Henderson

SPIE.

Benjamin D. Nation, Caleb L. Breaux, Peter J. Ludovice, Clifford L. Henderson, "Free energy of defects in chemoepitaxial block copolymer directed self-assembly: effect of pattern density and defect position," *J. Micro/Nanolith. MEMS MOEMS* **16**(4), 043501 (2017), doi: 10.1117/1.JMM.16.4.043501.

Free energy of defects in chemoepitaxial block copolymer directed self-assembly: effect of pattern density and defect position

Benjamin D. Nation,[a] Caleb L. Breaux,[a] Peter J. Ludovice,[a] and Clifford L. Henderson[a,b,c,*]
[a]Georgia Institute of Technology, Department of Chemical and Biomolecular Engineering, Atlanta, Georgia, United States
[b]Georgia Institute of Technology, Department of Chemistry and Biochemistry, Atlanta, Georgia, United States
[c]University of South Florida, Department of Chemical and Biomedical Engineering, Tampa, Florida, United States

Abstract. Block copolymers (BCPs) can phase separate to form periodic structures with small spacings, making BCPs an attractive option for furthering the ability of optical lithography. Chemoepitaxy is a method of directed self-assembly (DSA) that uses preferential pinning stripes to guide the BCP. The periodicity of the underlayers pinning stripe compared to the periodicity of the BCP is defined as the density multiplication. Molecular dynamics simulations are used to explore the effect that density multiplication and pinning stripe position (PSP) have on the free energy difference between a defective and defect-free BCP film. For all defect orders, the highest free energies were obtained when a pinning stripe was located directly under or adjacent to the terminating block. At high-density multiplications, the defects were found to approach the free energy of the same defect on an unpatterned underlayer. For all density multiplications and PSPs, the free energy of defective films is significantly higher than that of defect-free films, suggesting that the presence of defects in experiments is likely due to kinetic entrapment of defects. Free energy initially increases with increasing defect size but was found to level off and even decrease for the largest defects in this work. [DOI: 10.1117/1.JMM.16.4.043501]

Keywords: directed self-assembly; block copolymer; simulation; thermodynamic integration; defect; dislocation.

Paper 17056SSP received Apr. 28, 2017; accepted for publication Jul. 25, 2017; published online Oct. 20, 2017.

1 Introduction

As the semiconductor industry continues its attempt to follow Moore's law, the need for stringent uniformly spaced features grows. Some of the solutions to reaching higher feature densities have included e-beam lithography, nanoimprint lithography (NIL), extreme ultraviolet lithography (EUVL), and directed self-assembly of block copolymers (BCPs). While e-beam lithography has good control over feature sizes, it suffers from slow throughput and the need to write each individual pattern. NIL is relatively inexpensive and has increased throughput but not enough to meet the industry's requirements. In addition, NIL experiences high defectivity due to putting on and pulling off its imprint.[1] EUVL has the potential to reach very small sizes (down to 5 nm even) and is a promising route for improving the lithography process. While progress has been made in creating a high-intensity illumination source for EUVL, the process still suffers from its low intensity, resists used for the process, and ability to find and prevent mask defects.[2–5] As one of the solutions for achieving such small node sizes, BCPs have gained interest as self-assembling masks for subsequent etching or doping steps. A BCP is composed of two homopolymers that are joined by a covalent bond. This gives BCPs the ability to microphase separate into various geometries (i.e., spheres, cylinders, and lamellae) depending on the volume fraction of each block and the BCP's χN value. The product χN is the driving force for phase separation where N is the degree of polymerization and χ is a measure of the interactions between each block.[6,7] The semiconductor manufacturing industry intends to use BCPs by coating a thin film of BCP onto a substrate, allowing the BCP to self-assemble, selectively removing one of its blocks, and then using the remaining block as a mask to transfer the pattern to the substrate.[8–10] Lamellae and cylinder morphologies are of particular interest because they can create line/space or contact-hole patterns when etched. BCPs have been shown to phase separate into features with a sub-10-nm pitch (L_0, feature-to-feature spacing), an attractive quality for the goals set by the International Technology Roadmap for Semiconductors (ITRS).[11–15]

Supported thin films of lamellae forming BCP that are allowed to phase separate on unpatterned substrates form lamellae that lack long range order due to the effects of entropy in the system, thus creating what is commonly known as fingerprint patterns. While such patterns contain feature sizes that are of nanometer scale dimensions, they are not useful for the intended application of semiconductor device patterning due to the high level of disorder in such systems. As a result, some form of additional guidance must be provided to the BCP film that can suppress the entropic disorder in the system to produce long range ordered features. The two main forms of guidance are graphoepitaxy and chemoepitaxy. Graphoepitaxy works by using topography in the underlayer to constrain sections of BCP such that the most favorable condition for phase separation is a straight lamellae along the walls of the topography.[8,10,16] Chemoepitaxy, however, operates using an energetic contrast in the underlayer where typically a

*Address all correspondence to: Clifford L. Henderson, E-mail: clhenderson@usf.edu

1932-5150/2017/$25.00

highly preferential stripe "pins" down one block along a particular direction.[17–19] Adjacent to this "pinning stripe" is a region that is energetically neutral (if not slightly preferential to the nonpinned block) called the "background region." Typically the width of the pinning stripe (L_p) is half the natural pitch of the BCP, whereas the background region's width (L_b) may vary but usually satisfies the relation $L_b + L_P = n \cdot L_0$ such that the overall periodicity of the pattern is some integer (n) multiple of the natural pitch of the BCP. While the lowest amount of density multiplication (e.g., $n = 1$) gives the best pattern alignment due to the large number of pinning stripes, it does so at the cost of requiring the most lithographic effort. On the other hand, larger density multiplications are far easier lithographically, and, despite the absence of extra-periodic pinning stripes, these underlayers can still form well-aligned BCP films due to the BCPs desire to form defect-free lamellae.[20,21]

Despite the guidance by the underlayer, lamellae do not always form defect-free morphologies. Line defects such as dislocations and disclinations may form at the surface or in the through-film morphology. Experimentally, these defects occur at frequencies above the 1 defect per 100 cm^2 maximum that the ITRS desires.[22] The cause for the higher defect densities is thought to be one of the three sources: (1) non-BCP-related procedures, (2) the free energy of the defects are low enough that their equilibrium density is appreciable, or (3) the defects are kinetically trapped. In previous investigations into the free energy of defects, it was found that the relative-free energies for common simple defects such as dislocations were found to be above $300 \cdot k_B \cdot T$,[23,24] which yields a very low defect density using

$$\rho \propto \exp\left(\frac{-\Delta F}{k_B \cdot T}\right), \tag{1}$$

where ρ is the defect density, k_B is the Boltzmann constant, T is the temperature, and ΔF is the difference in the free energy of a defect versus the free energy of a defect-free state. While the relative-free energies for these defects are high, understanding how defect density, defect order (DO), and the pinning stripe's position relative to the defect affects the defect-free energy is still desirable. DO is defined here as the number of lamellae between the terminating blocks of the dislocation (indicated by the gray dots in Fig. 4). Coarse-grained molecular dynamic simulations were run on a BCP thin film atop various underlayers. Using thermodynamic integration, the relative-free energies were calculated for the various underlayer types and DOs.

2 Model Description

2.1 *Coarse-Grained Molecular Dynamics Model*

A previously developed coarse-grained molecular dynamics model is used in this work.[25,26] Each polymer is composed of unified beads or atoms that are each equivalent to four monomeric units. Polymers are coarse grained at this level since the statistical segment length of many common polymers, such as poly(styrene) and poly(methyl methacrylate), is less than four monomers. An illustration of this coarse-graining can be seen in Fig. 1(a). The beads in a polymer are connected to each other using a harmonic bond potential of the form

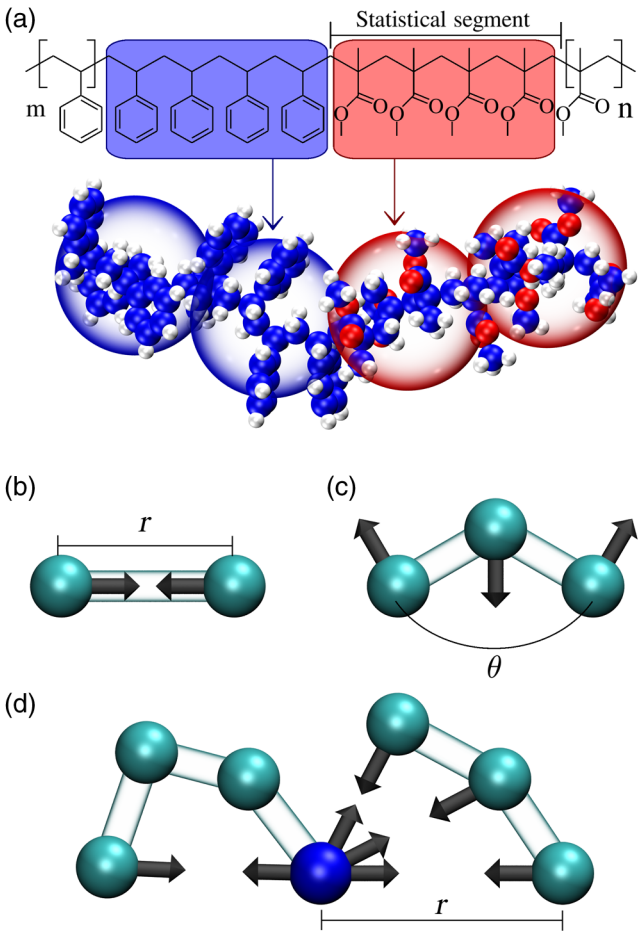

Fig. 1 (a) An illustration of the coarse-graining used in this work. Blue atomistic beads represent carbon, white represent hydrogen, and red represent oxygen. The blue and red transparent bubbles represent one coarse-grained polystyrene and poly(methyl methacrylate) bead, respectively. The coarse-grained bead is placed at the center of mass of the four monomeric units. Parts (b) through (d) show the force that the three potentials in this work apply to beads. (b) A harmonic bond potential is applied to every pair of bonded beads. (c) A harmonic angle potential is applied to every three consecutively bonded beads. (d) A nonbonded potential is applied to every pair of beads, excluding beads in the same bond or angle potential. In this case, the nonbonded forces between the dark blue bead and the other neighboring six beads shown are illustrated.

$$V_{\text{bond}} = \frac{1}{2} \cdot k_{\text{bond}} \cdot (r_{eq} - r)^2, \tag{2}$$

where V_{bond} is the harmonic bond potential energy, k_{bond} is the bond force constant, r_{eq} is the equilibrium bond length, and r is the measured length of the bond. An illustration of this force is shown in Fig. 1(b). For this work, $k_{\text{bond}} = 100$ kcal/mol and $r_{eq} = 0.82$ nm.

In addition to the bond potential, every three consecutively bonded beads have a harmonic angle potential acting on them of the form

$$V_{\text{angle}} = \frac{1}{2} \cdot k_{\text{angle}} \cdot (\theta_{eq} - \theta)^2, \tag{3}$$

where V_{angle} is the harmonic angle potential, k_{angle} is the angle force constant, θ_{eq} is the equilibrium angle between the three beads, and θ is the measured angle. An illustration

of this force is shown in Fig. 1(c). For this work, $k_{\text{angle}} = 5$ kcal/mol and $\theta_{eq} = \frac{2}{3} \cdot \pi$.

Except for bead pairs that already interact through a bond and/or an angle potential, every pair of beads experiences a nonbonded potential (i.e. a bead does not experience a nonbonded potential with a nearest neighbor or next-nearest neighbor bead, if they exist, on its polymer chain). The nonbonded potential is of the form

$$V_{ij}(r) = \varepsilon_{ij} \cdot \left[\left(\frac{\sigma_{ij}}{r} \right)^8 - 2 \cdot \left(\frac{\sigma_{ij}}{r} \right)^4 \right], \tag{4}$$

where V_{ij} is the nonbonded potential between beads of type i and j, ε_{ij} is the strength of the nonbonded interaction, σ_{ij} is the radius of the minimum energy, and r is the distance between two beads. An illustration of this force is shown in Fig. 1(d). For this work, $\sigma_{AA} = \sigma_{BB} = \sigma_{AB} = 1.26$ nm and $\varepsilon_{AA} = \varepsilon_{BB} = 0.5$ kcal/mol. The value of ε_{AB} is the primary parameter that controls χ. The value of the nonbonded potential is zero when beyond a cutoff radius of $R = 4$ nm. Each bead in the system has a mass of 418.4 Da. These parameters give homopolymers that are roughly equivalent to poly(styrene).

In this paper, during thermodynamic integration, ε_{AB} is varied from a starting value of $\varepsilon_{AB} = 0.5$ kcal/mol, where $\chi = 0$, to an ending value of $\varepsilon_{AB} = 0.35$ kcal/mol, where $\chi = 0.55$. The polymers used have a degree of polymerization (N) of 64 monomers (16 beads) making χN have a value of 35. The value of χ used here is larger than that of most BCPs currently used in the literature.[27] The free energy of defects has been shown to have a strong dependence on χ;[24] therefore, the free energy measured in this paper will likely be higher than most known BCPs. However, this higher value of χ should not affect how the free energy changes with the size of the defect and the design of the underlayer, which are the trends observed in this work.

Simulations are built using code written in MATLAB.[28] Molecular dynamics simulations are run using HOOMD-Blue on a GPU cluster.[29,30] Simulation results were viewed using code written in MATLAB.

Simulations in this work are composed of two pieces, the underlayer and the film. The underlayer is a brush underlayer, with each brush being a seven bead ($N = 28$) chain that has one end fixed in space. Brushes are placed with a brush density of 0.44 brushes/nm^2 and a square grid (leading to a grid spacing of 1.5 nm). A hard surface is simulated below the brushes by placing a second layer of fixed beads.[26] These fixed beads are located 0.83 nm beneath the brushes on a square grid that is offset from the brushes so that each bead is in the center of four brushes. This layer of fixed beads helps prevent any chains from inverting and facing downward into the substrate. The brush is composed of the same bead types as are used in the BCP film; however, they are labeled differently, so they do not experience the same external potentials that will be discussed later. To simulate chemoepitaxy, the underlayer types are assigned based on position. The underlayers being simulated are composed of an alternating pattern of a thin, highly preferential pinning stripe, and a wider neutral region. The pinning stripes are always $0.5 \cdot L_0$ wide, whereas the background region is $(n - 0.5) \cdot L_0$ wide, where n is the degree of density multiplication. In this work, the background region is always composed of 50% A beads and 50% B beads. The pinning stripe is always 100% of either A or B beads depending on which bead type needs to be the pinning type for the simulation. Illustrations of three of these underlayers are shown in Fig. 2. Figure 2(a) shows an 8× density multiplying underlayer with its only pinning stripe located at position 0 (the center of the defect). Figure 2(b) shows the same density multiplication but with the pinning stripe in position 2 (two lamellae from the center of the defect). Figure 2(c) shows the same pinning stripe position (PSP) as Fig. 2(b) but on a 4× density multiplying underlayer that has an additional pinning stripe located at position −6.

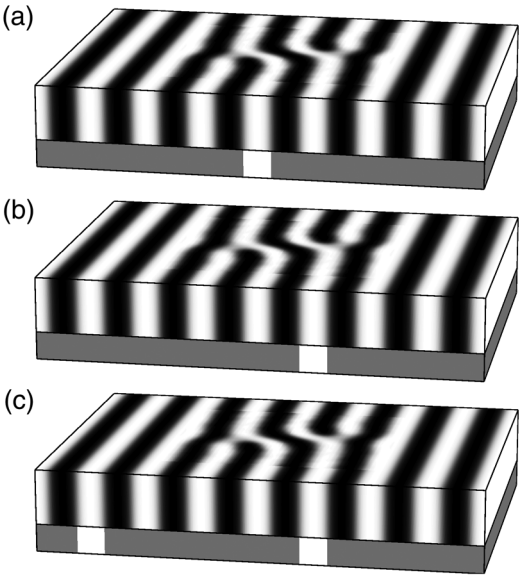

Fig. 2 Illustrations of three different patterned underlayers used in this work. The top portion of each illustration is the BCP film with a dislocation of order 1. The bottom portion represents the brush underlayer. The background region is represented by the gray region and is neutral to both the white and black blocks of the BCP. The pinning stripe is the white region and is highly preferential to the white block of the BCP. (a) An 8× density multiplying underlayer with pinning stripe position 0. (b) An 8× density multiplying underlayer with pinning stripe position 2. (c) An 4× density multiplying underlayer with pinning stripe position 2.

BCP films are generated by creating chains using a random walk. The chains are then randomly placed with their center of mass inside a simulation box with dimensions of the desired film until the appropriate density is reached. For the polymer used here, the density is 1.35 beads/nm^3. Next, the BCP chains are periodically wrapped in the x- and y-dimensions. Finally, the film is placed on top of the desired underlayer. These films are initially well mixed. The majority of films were built with dimensions of $8 \cdot L_0 \times 6 \cdot L_0 \times 0.75 \cdot L_0$, where L_0 is the pitch of the BCP, which is 11.8631 nm for this BCP.

Simulations undergo two minimization steps after being built. The first minimization gently pushes apart beads that were placed too close together initially. To do this, σ_{ij} is initially set to a very low value, which prevents beads from feeling too high of a force from the highly repulsive regime of the nonbonded potential. A series of short minimizations (50 steps each) are run, increasing σ_{ij} in each run until the desired value is reached. Minimizations are run using the HOOMD FIRE minimizer (parameters: $dt = 5 \times 10^{-6}$,

ftol $= 1 \times 10^{-2}$, Etol $= 1 \times 10^{-7}$, finc $= 1.99$, fdec $= 0.8$, alpha_start $= 0.01$, and falpha $= 0.9$).

The second minimization step is a more generic minimizer run at the final parameter values. This minimization runs for 20,000 steps using the FIRE minimizer with parameters dt $= 5 \times 10^{-4}$, ftol $= 1 \times 10^{-2}$, and Etol $= 1 \times 10^{e-7}$. After completing both minimizations, a brief simulation is run with $\chi = 0$ for 200,000 timesteps (10 ns) to collapse the film to the brush underlayer and allow the film to better equilibrate, eliminating any unrealistic density fluctuations generated during the initial build. This simulation is run with the HOOMD standard NVT integrator, which uses a Nose–Hoover thermostat. For these simulations, the temperature set point is $T = 500$ K, the controller coupling constant is tau $= 0.2$ timesteps, and the integration timestep is 0.05 ps.

2.2 *Thermodynamic Integration*

Thermodynamic integration is a method that can be used to calculate the free energy difference between two different states in a molecular dynamics simulation. In thermodynamic integration, the molecular dynamics simulation is brought from one state to another in a reversible manner. In this paper, thermodynamic integration is used to calculate the difference in the free energy of a defective BCP film versus a defect-free lamellar state. The thermodynamic path used is summarized in Fig. 3. A simulation is started in the mixed state at $\chi = 0$. This simulation is then phase separated using only an external potential by ramping the strength of the external potential from $A = 0$ to $A = 1$. Next χ is ramped from a value of $\chi = 0$ to $\chi = 0.55$. Finally, the external potential is turned off (by ramping $A = 1$ to $A = 0$). This is performed once using a defect-free external potential and a second time using a defect external potential.

The external potential used to generate defect-free lamellae is given by the following equation:

$$V(x) = A \cdot \frac{\tanh\left[\frac{1}{2\pi w}\cos\left(\frac{2\pi}{L_0}\cdot x\right)\right]}{\tanh\left[\frac{1}{2\pi w}\right]}, \tag{5}$$

where V is the external potential, A is the magnitude of the external potential, w is related to the width of the interface and is given a value of 0.1, and L_0 is the pitch of the BCP. This potential was found to reproduce defect-free lamellae well. This potential can be seen in Fig. 4 in the defect-free case, as well as in the area outside the gray boxes in all the other potentials. The numbers at the bottom represent the relative position of each lamellae (normalized by $0.5 \cdot L_0$) to the center of the defect. Due to the symmetry of the defect, pinning stripes at equal distances to the center of the defect but on opposite sides of the center are considered equivalent. The external potential used to generate defective lamellae requires the use of a table potential, which can be seen inside the gray box in Fig. 4. The tables for these defects were generated using a defect that formed naturally in a previously run simulation that started from a mixed state and was allowed to undergo phase separation on its own (i.e., without the aid of an external potential). The defect used naturally occurred and persisted for a long period of time. To generate the defect table, snapshots were taken of the simulation through time. These snapshots were then averaged through time to generate the average defect state. It was then assumed that the volume fraction could be related to the potential directly. The tables used had a node spacing of $0.08 \cdot L_0$ with bicubic interpolation being used between nodes.

In the first branch, the external potential is turned on by ramping A from $A = 0$ to $A = 1$. It was found that $A = 1$ is a sufficient strength for the external potential to fully phase separate the BCP film. The external potential was turned on in 50 steps, with a stepsize of $\Delta A = 0.02$. Each step in A was run for 1,000,000 timesteps or 50 ns. It was found that equilibrium was typically reached within the first few nanoseconds. The external potential in the simulation was then logged every 100 timesteps. The external potential energy was averaged over the final 45 ns of each step. The integral in Eq. (6) was then evaluated using the trapezoidal rule.

$$\Delta F_1^i = \int_{A=0}^{A=1} \frac{\langle V_{\text{ext}}(A)\rangle}{A}\,\mathrm{d}A, \tag{6}$$

where ΔF_1^i is the free energy difference between the beginning and ending state of the first branch and $\langle V_{\text{ext}}(A)\rangle$ is the average external potential measured when the external strength is A. Here, and for the remaining ΔF's, the superscript i will represent which path the integration is taking (to a defective or a defect-free state).

The second branch ramps on χ while keeping the external potential at full strength. The value of ε_{AB} is decreased in this branch in increments of $\Delta\varepsilon_{AB} = 0.005$ kcal/mol. Each step in ε_{AB} is run for 80,000 timesteps or 4 ns. Every 100 timesteps the nonbonded potential between A and B beads is measured. This value is averaged over the final 2.5 ns to give $\langle V^{AB}_{\text{non-bonded}}(\varepsilon_{AB})\rangle$, which is then used in the following integral to get the free energy of this branch:

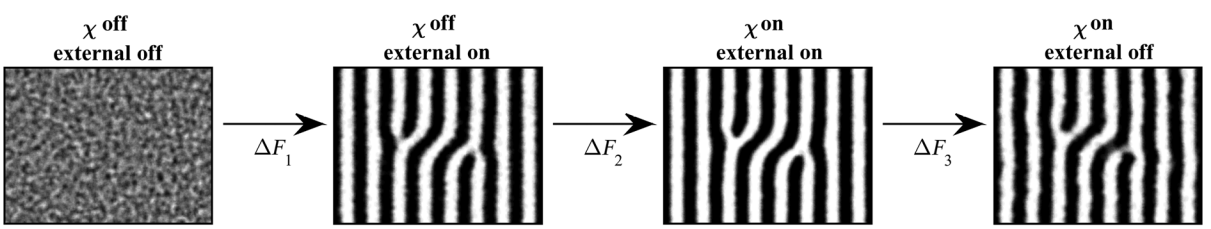

Fig. 3 Images of the thermodynamic integration pathway used. Simulations start in a mixed state and then phase separated using an external potential. In the next branch, χ is turned on, which primarily just sharpens the interfaces. Finally, the external potential is turned off, which allows the film to relax and reach its equilibrium state.

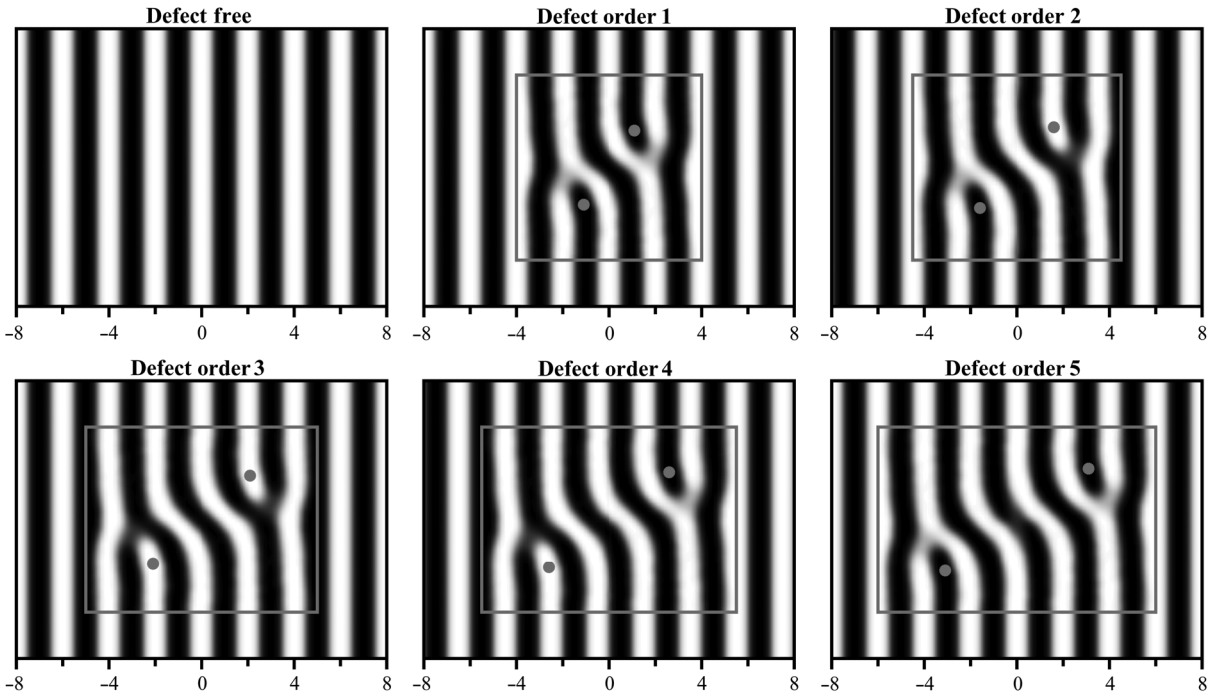

Fig. 4 All external potentials used in this paper. The portion of the external potential outside the gray box is generated using Eq. (5), while the area inside is generated using a table lookup that is interpolated with bicubic interpolation. The dislocation order indicates the number of lamellae between the two terminating blocks in the film, which are indicated by the gray dots. The *x*-axis indicates the position relative to the center of the defect, which is in units of number of lamellae.

$$\Delta F_2^i = \int_{\varepsilon_{AB}=0.5}^{\varepsilon_{AB}=0.35} \frac{\langle V^{AB}_{\text{non-bonded}}(\varepsilon_{AB})\rangle}{\varepsilon_{AB}} d\varepsilon_{AB}, \tag{7}$$

where ΔF_2^i is the free energy difference over the second branch. This branch requires less timesteps at each step in ε_{AB} because little bulk rearrangement is happening in the film during this time. Instead, the primary changes noticed are a sharpening of the interfaces between lamellae.

The final branch ramps down the external potential strength. The value of A is decreased from $A = 1$ to $A = 0$ in 30 steps. Each step in A is run for 80,000 timesteps or 4 ns. Every 100 timesteps the nonbonded potential between A and B beads is measured. This value is averaged over the final 2.5 ns to give $\langle V_{\text{ext}}(A)\rangle$, which is then used in the following integral to get the free energy of this branch:

$$\Delta F_3^i = \int_{A=1}^{A=0} \frac{\langle V_{\text{ext}}(A)\rangle}{A} \mathrm{d}A, \tag{8}$$

where ΔF_3^i is the free energy difference over the third branch. Like the second branch, less timesteps at each step is required because little bulk rearrangement is happening in the film.

The difference in free energy of one path versus another is given by the following equation:

$$\Delta F_j = \Delta F_j^{M\to D} - \Delta F_j^{M\to DF}, \tag{9}$$

where ΔF_j is the difference in free energy of one branch for one path versus another. The two paths are from a mixed state to a defect state ($M \to D$) and from a mixed state to a defect-free state ($M \to DF$). This value is useful since it shows how much contribution to the overall free energy difference each branch had. The overall difference in free energy, ΔF, is then determined by adding the three branches,

$$\Delta F = \Delta F_1 + \Delta F_2 + \Delta F_3. \tag{10}$$

Thermodynamic integration is a useful tool for measuring free energy in molecular dynamics models. However, there are a few significant drawbacks. First, as is the case in all free energy models, the size of the simulation volume can affect the free energy of the system.[23] This effect is lessened by using larger simulation volumes. Second, thermodynamic integration gives increases in accuracy by increasing the number of integration steps and by increasing the number of timesteps to average over at each integration step. Both of these methods of increasing the accuracy of free energy measurements involves a significant increase in simulation time. In addition, in this work there is the possibility that a defect will anneal out of a film (leaving the film in a defect-free state) when the external potential is turned off. While the defect annealing is a rare event, if the simulation is run longer (to increase the accuracy of the measurement), then the likelihood of this rare event occurring increases. When the defect does anneal, it violates reversibility, invalidating the free energy measurement.

3 Results and Discussion

3.1 *Pinning Stripe Location*

Figure 5 shows the free energy difference for an 8× density multiplying underlayer for various PSPs. In these cases, there

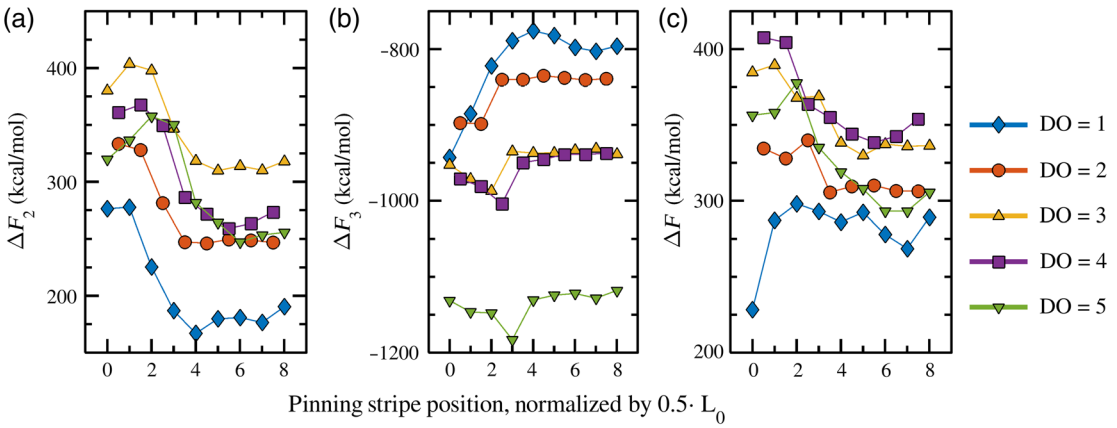

Fig. 5 Plots showing (a) the second branch of the free energy calculation, (b) the third branch of the free energy calculation, and (c) the total free energy difference between the defect and a defect-free state versus the position of the pinning stripe for an 8× density multiplying underlayer.

is only one pinning stripe in the system. The position of the pinning stripes is their distance from the center of the defect (divided by $0.5 \cdot L_0$), as shown in Fig. 4. It should be noted that the odd numbered defects have pinning stripes centered on integer values (n), while even numbered defects have pinning stripes on the half values ($n + 0.5$). The individual branches of the thermodynamic integration for the second branch (ramping up χ) and third branch (turning off the external potential) are shown in Figs. 5(a) and 5(b), respectively, whereas the overall free energy difference is shown in Fig. 5(c). The first branch of the integration is not plotted since ΔF_1 is not a function of pinning stripe location. This is because the entire first step is done with $\chi = 0$, so there is no differentiation between underlayer beads. The values of ΔF_1 are 895, 898, 957, 1018, and 1168 kcal/mol for defects of order 1, 2, 3, 4, and 5, respectively. All points shown in the figure and the data point mentioned above are the average of three replicates.

Looking at the overall free energy in Fig. 5(c), it can be seen that the dislocations have similar trends with the exception of the dislocation with a DO of 1. This is due to many DO = 1 simulations annealing out during the third branch, that is to say, the defects were annihilated, leaving behind straight lamellae. While defect annihilation (as well as defect growth) is possible for all DOs, it was only observed in the DO = 1 case due to the close proximity of the pair of dislocations of which DO = 1 is composed. Due to this close proximity, one dislocation will "feel" when the shape of the other dislocation is perturbed by a nearby pinning stripe. For a larger DO, there are multiple lamellae separating the dislocations that damp out the perturbation from the pinning stripe. However, in the DO = 1 case, there is little material to damp it out. While a dislocation pair can withstand some perturbation in one dislocation, when both are altered, it becomes far more likely that the dislocation will change in order.

The effect of DO = 1 annealing out in the third branch when a pinning stripe is close can be seen in the third branch of the thermodynamic integration [Fig. 5(b)]. During the third branch, there should be almost no rearrangement of beads in the system if the defect that was built using the external potential is close to the true equilibrium defect shape. If there is no rearrangement, the third branch should be constant with respect to the PSP. This is approximately the case for all defects other than DO = 1, as will be discussed further later. As mentioned before, when the pinning stripe approaches the center of DO = 1, the defect will frequently anneal out while ramping down the external potential. This spontaneous transition violates reversibility, which invalidates the free energy measurement from thermodynamic integration in these cases.

On the other hand, for defects other than DO = 1, the third branch is mostly constant with respect to PSP. There are some variations, in particular, a lowering of ΔF_3 when the pinning stripe approaches the terminating block of the defect. In these cases, the defect will necessarily adapt its shape slightly to accommodate the pinning stripe. However, these variations are small in magnitude and gradually happen in a reversible manner, allowing thermodynamic integration to still be valid. Since the ΔF_3 is roughly constant with regard to PSP, and what few variations are present appear small, it can be assumed that the second branch of the integration, ΔF_2, is the primary contributor to the total free energy with respect to the PSP. Therefore, while the total free energy of DO = 1 is likely invalid, the second branch of the integration can be looked at as a proxy for the total free energy.

A few observations can be made by analyzing the second branch of the integration [Fig. 5(a)]. First, as the pinning stripe moves further from the defect, toward higher PSP values, the free energy begins to level off at its minimum value. This is due to the pinning stripe interacting less and less with the defect and, therefore, having a negligible effect on the free energy. The PSP where the free energy levels off increases with an increasing DO but appears to be within $0.5 \cdot L_0$ of the terminating block. While DO = 1 seems to level off around PSP = 3, each increase in DO seems to increase this transition by approximately 0.5 PSP. This suggests that pinning stripes beyond a distance of L_0 outside of the terminating block (marked by the gray dots in Fig. 4) have little effect on the free energy of the defect.

As the pinning stripe approaches the defect, the free energy greatly increases due to the increased interactions of the pinning stripe with the defect. The magnitude of this increase is on the order of 50 to 100 kcal/mol, implying that these defects will almost never occur naturally above the pinning stripe at equilibrium.

For some of the larger defects, such as DO = 3 or 5, there appears to be a maximum in the free energy when the pinning stripe is not at the center of the defect (PSP = 0). The position of these maximums are roughly PSP = 1 and 2 for DO = 3 and 5, respectively, implying that the maximum likely shifts further right as the DO is increased. The location of the maximum corresponds to the lamellae interior to the terminating block of the defect, which is at PSP = 2 and 3 for DO = 3 and 5, respectively. Since the pinning stripe being directly under or on the interior of the terminating block consistently gives the maximum in free energy, it suggests that a pinning stripe in these locations destabilizes the defect. This pinning stripe location also likely has the highest kinetics for defect annihilation since a pinning stripe in this location will increase the likelihood of bridge formation, which is a necessary step in defect annihilation.[31]

The location where the free energy levels off can be a good approximation for what density multiplication is large enough to allow the defect to form. For example, since DO = 1 levels off around PSP = 3, it can be assumed that this dislocation is more likely to form if the density multiplication is 3× or greater since the defect can form entirely between two pinning stripes. However, if the density multiplication is less than 3×, then there is guaranteed to be a pinning stripe in either PSP = 0, 1, or 2, which are in the increased free energy region. Similarly, for DO = 3 the free energy levels off around PSP = 4, and for DO = 5 it levels off around PSP = 5. This implies that decreasing the density multiplication should decrease the number of the larger defects significantly. However, since the maximum in the free energy is not at PSP = 0 for these larger defects, there exists the possibility of a dislocation pair that straddles a pinning stripe. For example, with DO = 5, if the pinning stripe is at PSP = 0, the dislocation pair can fit nicely on a 3× underlayer with one pinning stripe in the center of the defect and another two on the outside of the dislocation pair (at positions −6 and +6). This particular example defect has been naturally observed in simulations using this model and has been shown to be very stable since the defect persisted without changing the DO for very long simulation times.

Looking at the overall free energy, ΔF, Fig. 5(c), where the pinning stripe is far from the defect (approaching PSP = 8), it can be seen that the free energy is lowest for DO = 1, increases for DO = 2, increases further for DO = 3, stays approximately the same for DO = 4, and then decreases for DO = 5. It is hypothesized that this trend is due to two competing factors. First, increasing the DO increases the amount of curvature in the BCP system, which enthalpically would increase the free energy. Second, the two halves of the dislocation pair likely destabilize each other when they are too close. This hypothesis would lead to the observed results where initially the free energy increases from defect free to DO = 1 to DO = 3 due to the increasing interfacial area. When DO = 4 is reached, the increase in interfacial area is counteracted by the stabilizing effect of the dislocation pairs being further separated. Finally, with DO = 5, the defect begins to get more stable due to the further separation of the dislocation pairs. This has large practical consequences on defect annihilation kinetics. If it is assumed that the pathway to annealing DO = 5 is for the defect to first shrink to DO = 4, then to DO = 3, and so on, as has been observed in simulation,[31,32] then DO = 4 could be considered a transition state in the process of annealing DO = 5 to a defect-free state. While DO = 5 has a much higher free energy than defect free (≈300 kcal/mol) and should therefore be virtually nonexistent at equilibrium, the fact that the transition state DO = 4 has a far higher free energy (≈340 kcal/mol) suggests that there will be very slow kinetics in annealing out DO = 5. These data help support the theory that defects in BCP films are kinetically trapped.

It has been shown that thermodynamic integration simulations can suffer from a limited simulation volume.[23] This was a concern, particularly for the larger DOs since it is more likely that the defect could see itself across the periodic boundary. However, it should be noted that the presence of a pinning stripe near the periodic boundary of the system lessens this concern since the pinning stripe decreases the amount a defect could influence itself across the boundary. To test the simulation volume effect, a limited number of larger simulations were run. These larger simulations were $12 \cdot L_0$ wide, while the typical simulations were only $8 \cdot L_0$ wide. These larger simulations took roughly 1.5 times as long as the smaller simulations. A single replicate was run for DOs 3, 4, and 5 where the size effect should be most apparent. This is also where the free energy begins to level off and then decrease, as detailed in the previous paragraph, so these larger simulations should help verify that trend. An underlayer with 12× density multiplication was used, with the pinning stripe located away from the defect on the edge of the simulation. The results of the larger volume simulations showed the same general trends as were observed in the smaller simulations, with DO = 3 and DO = 4 having roughly equivalent free energies ($\Delta F = 256$ and $\Delta F = 250$ kcal/mol, respectively) and DO = 5 having significantly lower free energy ($\Delta F = 170$ kcal/mol). However, while the trend is the same, the absolute values of the free energy differences were approximately 100 kcal/mol lower than before. This suggests that the smaller simulations are indeed experiencing this size effect; however, it appears they do capture trends accurately.

3.2 *Density Multiplication*

Underlayers with 1×, 2×, 4×, and 8× density multiplication were simulated. In addition, an unpatterned underlayer was simulated to approximate an infinite density multiplication. These results are shown in Fig. 6 where the free energy differences between a defective film and a defect-free film are shown for various DOs as a function of density multiplications. The points shown for each density multiplication are the free energy difference corresponding to the lowest average free energy over all PSPs for that density multiplication. It can be seen that, as the density multiplication increases, the difference in free energy decreases. This is due to higher density multiplications having less pinning stripes per area and, therefore, a lowered driving force for pattern correction when a defect is present. Intuition would suggest that the free energy difference should asymptotically approach the unpatterned (infinite density multiplication) case as the density multiplication increases, which appears to be the case in these simulations.

Assuming a Boltzmann's distribution, the defect density can be estimated using the free energy difference and Eq. (1). From Fig. 6, these free energy differences can be used to determine what the return is for putting in the increased

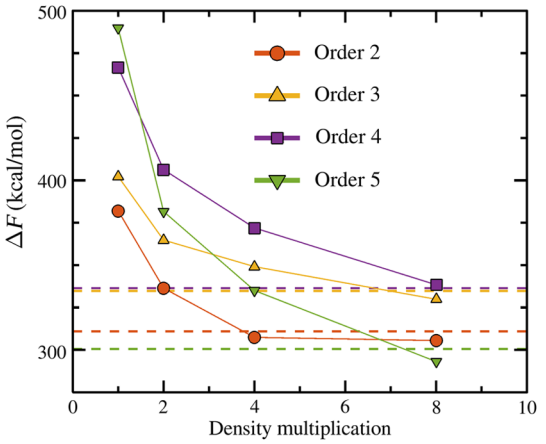

Fig. 6 Free energy differences for thermodynamic integration for various density multiplications. Each point represents the minimum free energy difference of all pinning stripe positions for that density multiplication. The horizontal dashed lines near the bottom represent the free energy difference of the defect measured on an unpatterned underlayer.

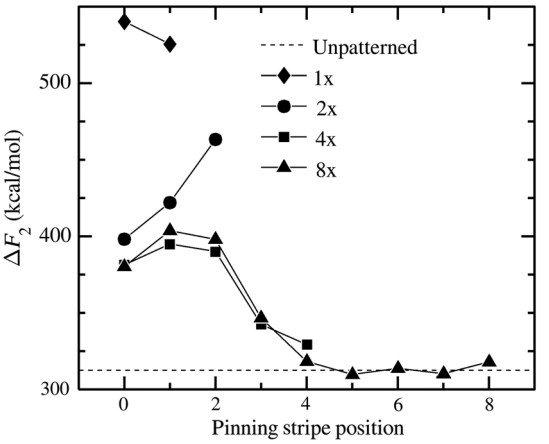

Fig. 7 Free energy differences for the second branch in the thermodynamic integration for DO = 3. The unpatterned underlayer free energy is represented by a horizontal dashed line at the bottom of the graph.

lithographic effort to make a more highly defined underlayer pattern. For instance, for DO = 5, the difference in free energy between 1× and 2× density multiplication is approximately 100 kcal/mol. Since in these simulations $k_B \cdot T \approx 1$ kcal/mol, it is e^{100} times more likely to find this defect on a 2× density multiplication than 1×. This type of comparison can be useful when looking at higher density multiplications to determine when increasing density multiplication will no longer have an effect on the equilibrium defect density. For all defects shown here, the 8× underlayers had nearly the same defect-free energy difference as the unpatterned cases, meaning that at equilibrium the defect density for any density multiplication greater than 8× will all be nearly the same. With the exception of DO = 2, decreasing the density multiplication from 8× to 4× increased the free energy difference by 20 kcal/mol or more. This suggests that these defects will occur at least 5×10^8 times more on an 8× underlayer than a 4× underlayer. On the other hand, for DO = 2, the defects are still small enough that a decrease in density multiplication from 8× to 4× has no effect on the free energy, and even higher smaller density multiplications would be needed to affect the free energy.

Figure 7 takes a closer look at the effect of density multiplication in regard to PSP for DO = 3 by looking at the second branch of thermodynamic integration. The previous section has already discussed the 8× underlayers and has explained why having a pinning stripe in positions 1 or 2 (PSP = 1 or PSP = 2) has the highest free energy difference due to its proximity to the terminating block. As the density multiplication decreases, the number of pinning stripes present in the underlayer increases. For 4× underlayers, there are two pinning stripes throughout our simulation, yet the 4× underlayers mostly follow the same trend as 8× underlayers. This implies that the extra-pinning stripe is still too far away from the defect's terminating blocks to cause it any substantial instability.

For 2× underlayers, four pinning stripes are present in the simulations underlayer. It can be seen that the free energy significantly increases as the PSP shifts to the right. This trend can be explained by looking at the locations of all the pinning stripes in the system, but especially the two closest to the defects terminating blocks. For 2× density multiplication, the pair of pinning stripes are always PSP = x and PSP = $x \pm 4$ (see Fig. 4, Defect Order 3 for reference). In the case of PSP = 0 and ±4, the closest distance from one pinning stripe to a terminating block is relatively far (L_0). On the other hand, PSP = 1 and −3 has both pinning stripes $0.5 \cdot L_0$ away from the terminating block (one on the inside and one on the outside). While in the 8× simulations, a pinning stripe in position 3 does not significantly increase the free energy, a pinning stripe in position 1 does, which explains why this point is higher in free energy than PSP = 0 and ±4. A similar analysis can be done for PSP = 2 and −2. Since both of these pinning stripes are beneath a terminating block, and from the 8× simulations we see that this is near where the maximum in the free energy occurs, it follows that this underlayer would have the highest free energy of the 2× underlayers.

A similar analysis can be performed for the 1× underlayer. In this case, the nearest pinning stripes are at PSP = $x \pm 2$. Using this, when PSP = 0 and ±2, there are two pinning stripes directly underneath the terminating block as well as one pinning stripe in the center of the defect, which greatly contributes to increasing the free energy. When PSP = −3, −1, 1, and 3 while there are two pinning stripes in highly unfavorable spots (PSP = ±1), the two other pinning stripes are getting to the region where they will have less effect on the free energy, causing this position to have an overall lower free energy.

4 Conclusions

Molecular dynamics simulations were implemented to determine the effect that the pinning stripe and density multiplication have on the free energy of dislocation defects of various orders. For all DOs, it was found that the free energy was generally highest when the terminating block of a dislocation was situated above a pinning stripe, suggesting that there is little probability of the defect being positioned in these locations at equilibrium. It was found that pinning stripes approximately $1 \cdot L_0$ outside of the terminating blocks of the defect have little effect on the free energy of the defect. If the defect is large enough, there exists a

location in the center of the defect where pinning stripes have less of a free energy penalty than underneath the terminating block, suggesting that defects can be stable while straddling a pinning stripe. For the defects explored here, when the density multiplication was 8×, the thermodynamic driving force for the removal of the defects simulated here was approximately the same as for unpatterned underlayers because the defect was able to fit in an area without a pinning stripe nearby. While increasing density multiplication does theoretically increase the number of defects present due to a decreased free energy difference, the free energy difference is still incredibly high even on an unpatterned underlayer, making their estimated population very small. This bolsters the idea that the high defect densities reported experimentally are due to kinetic entrapment. Increasing the DO does not appear to increase the free energy monotonically. Instead, a defect of order 5 appears to have a lower free energy than a defect of order 3. It is hypothesized that free energy versus DO is controlled by two competing factors: the increase in interfacial area for larger defects increases free energy, while the greater separation of the dislocation pairs decreases free energy by stabilizing each dislocation.

Acknowledgments

The authors would like to thank Intel for funding the purchase of the computer cluster used for this work. This material was based upon work supported by the National Science Foundation under Grant No. CMMI-1534461 and Grant No. CBET-1512517. Any opinions, findings, and conclusions or recommendations expressed in this material are those of the author(s) and do not necessarily reflect the views of the National Science Foundation.

References

1. S. Barcelo and Z. Li, "Nanoimprint lithography for nanodevice fabrication," *Nano Convergence* **3**, 21 (2016).
2. Z. J. Qi et al., "Toward defect-free fabrication of extreme ultraviolet photomasks," *J. Micro/Nanolithogr., MEMS, MOEMS* **15**(2), 023502 (2016).
3. A. De Silva et al., "Single-expose patterning development for EUV lithography," *Proc. SPIE* **10143**, 101431G (2017).
4. J. Schoot and H. Schift, "Next-generation lithography–an outlook on EUV projection and nanoimprint," *Adv. Opt. Technol.* **6**(3–4), 159–162 (2017).
5. S. Singh et al., "A study on EUV reticle surface molecular contamination under different storage conditions in a HVM foundry fab," *Proc. SPIE* **10143**, 101431T (2017).
6. F. S. Bates and G. H. Fredrickson, "Block copolymer thermodynamics: theory and experiment," *Annu. Rev. Phys. Chem.* **41**(1), 525–557 (1990).
7. M. Matsen et al., "Conformationally asymmetric block copolymers," UMSI research report, University of Minnesota, Supercomputer Institute, Minneapolis, Minnesota, Vol. **96**, 125 (1997).
8. J. Kim et al., "Toward high-performance quality meeting IC device manufacturing requirements with AZ SMART DSA process," *Proc. SPIE* **9423**, 94230R (2015).
9. S. Ji et al., "Directed self-assembly of block copolymers on chemical patterns: a platform for nanofabrication," *Prog. Polym. Sci.* **54**, 76–127 (2016).
10. R. A. Segalman, "Patterning with block copolymer thin films," *Mat. Sci. Eng.* **48**(6), 191–226 (2005).
11. T. Ghoshal et al., "Fabrication of ultra-dense sub-10 nm in-plane Si nanowire arrays by using a novel block copolymer method: optical properties," *Nanoscale* **8**, 2177–2187 (2016).
12. T. Seshimo et al., "Perpendicularly oriented sub-10-nm block copolymer lamellae by atmospheric thermal annealinng for one minute," *Sci. Rep.* **6**, 19481 (2016).
13. K. Aissou et al., "Sub-10 nm features obtained from directed self-assembly of semicrystalline polycarbosilane-based block copolymer thin films," *Adv. Mater.* **27**(2), 261–265 (2015).
14. N. Kihara et al., "Sub-10-nm patterning process using directed self-assembly with high block copolymers," *J. Micro/Nanolithogr., MEMS, MOEMS* **14**(2), 023502 (2015).
15. W. J. Durand et al., "Design of high-χ block copolymers for lithography," *J. Polym. Sci., Part A: Polym. Chem.* **53**(2), 344–352 (2015).
16. C. Cummins et al., "Solvothermal vapor annealing of lamellar poly(styrene)-block-poly(d, l-lactide) block copolymer thin films for directed self-assembly application," *ACS Appl. Mater. Interfaces* **8**(12), 8295–8304 (2016).
17. L. D. Williamson et al., "Three-tone chemical patterns for block copolymer directed self-assembly," *ACS Appl. Mater. Interfaces* **8**(4), 2704–2712 (2016).
18. W. Li and M. Müller, "Directed self-assembly of block copolymers by chemical or topographical guiding patterns: optimizing molecular architecture, thin-film properties, and kinetics," *Prog. Polym. Sci.* **5455**, 47–75 (2016).
19. T. Chang et al., "Directed self-assembly of block copolymer films on atomically-thin graphene chemical patterns," *Sci. Rep.* **6**, 31407 (2016).
20. R. Ruiz et al., "Density multiplication and improved lithography by directed block copolymer assembly," *Science* **321**(5891), 936–939 (2008).
21. C. Liu et al., "Chemical patterns for directed self-assembly of lamellae-forming block copolymers with density multiplication of features," *Macromolecules* **46**(4), 1415–1424 (2013).
22. H. Pathangi et al., "DSA materials contributions to the defectivity performance of 14nm half-pitch line flow at IMEC," *Proc. SPIE* **9777**, 97770G (2016).
23. U. Nagpal et al., "Free energy of defects in ordered assemblies of block copolymer domains," *ACS Macro Lett.* **1**(3), 418–422 (2012).
24. A. J. Peters et al., "Calculations of the free energy of dislocation defects in lamellae forming diblock copolymers using thermodynamic integration," *J. Micro/Nanolithogr., MEMS, MOEMS* **15**(2), 023505 (2016).
25. R. A. Lawson et al., "Coarse grained molecular dynamics model of block copolymer directed self-assembly," *Proc. SPIE* **8680**, 86801Y (2013).
26. A. J. Peters et al., "Detailed molecular dynamics studies of block copolymer directed self-assembly: effect of guiding layer properties," *J. Vac. Sci. Technol., B* **31**, 06F302 (2013).
27. C. Sinturel, F. S. Bates, and M. A. Hillmyer, "High χ low N block polymers: how far can we go?" *ACS Macro Lett.* **4**(9), 1044–1050 (2015).
28. *MATLAB, Version 8.6.0 (R2015b)*, The MathWorks Inc., Natick, Massachusetts (2015).
29. J. Glaser et al., "Strong scaling of general-purpose molecular dynamics simulations on GPUs," *Comput. Phys. Commun.* **192**, 97–107 (2015).
30. J. A. Anderson, C. D. Lorenz, and A. Travesset, "General purpose molecular dynamics simulations fully implemented on graphics processing units," *J. Comput. Phys.* **227**(10), 5342–5359 (2008).
31. A. J. Peters et al., "Coarse-grained molecular dynamics modeling of the kinetics of lamellar block copolymer defect annealing," *J. Micro/Nanolithogr., MEMS, MOEMS* **15**(1), 013508 (2016).
32. S. Hur et al., "Molecular pathways for defect annihilation in directed self-assembly," *Proc. Natl. Acad. Sci. U. S. A.* **112**(46), 14144–14149 (2015).

Benjamin D. Nation completed his BSc(Hons) degree in chemical engineering at Tennessee Technological University in 2012. He is a PhD candidate at Georgia Institute of Technology under the advisement of professor Clifford L. Henderson and professor Peter J. Ludovice at Georgia Institute of Technology. His research is on the simulation of block copolymer directed self-assembly.

Caleb L. Breaux completed his BSc degree in chemical engineering at the University of Louisana at Lafayette in 2012. Currently, he is progressing through his PhD under professors Clifford L. Henderson and Pete J. Ludovice at Georgia Institute of Technology. Research interests include synthesis of new BCP materials and their DSA as well as the effect of thin film conditions on BCP defectivity.

Peter J. Ludovice is an associate professor of chemical engineering at Georgia Institute of Technology. After completing his BS degree and PhD in chemical engineering from the University of Illinois and MIT, respectively, he carried out molecular modeling research at the ETH-Zürich, IBM, NASA, and Molecular Simulations Inc. (now BIOVIA). His current research focuses on the computer simulation of synthetic and biological macromolecules.

Clifford L. Henderson is a professor in the School of Chemical and Biomolecular Engineering at the Georgia Institute of Technology and an adjunct professor in the School of Chemistry and Biochemistry at Georgia Tech. He received his BSc degree in chemical engineering with highest honors from Georgia Institute of Technology and his MSc degree and PhD in chemical engineering from the University of Texas at Austin.